



# Ferrimagnetic spintronics

Se Kwon Kim<sup>1</sup>, Geoffrey S. D. Beach<sup>2</sup>, Kyung-Jin Lee<sup>1,3,4</sup>✉, Teruo Ono<sup>5,6</sup>, Theo Rasing<sup>7,8</sup> and Hyunsoo Yang<sup>9</sup>

**Ferrimagnets composed of multiple and antiferromagnetically coupled magnetic elements have attracted much attention recently as a material platform for spintronics. They offer the combined advantages of both ferromagnets and antiferromagnets, namely the easy control and detection of their net magnetization by an external field, antiferromagnetic-like dynamics faster than ferromagnetic dynamics and the potential for high-density devices. This Review summarizes recent progress in ferrimagnetic spintronics, with particular attention to the most-promising functionalities of ferrimagnets, which include their spin transport, spin texture dynamics and all-optical switching.**

Ferrimagnets are a class of magnets with unbalanced antiparallel-aligned sublattice moments, which results in a finite, albeit small, magnetization (Fig. 1a). The term ‘ferrimagnetism’ was originally introduced<sup>1</sup> to describe the small net magnetization in ferrites where Fe moments in two inequivalent sites couple antiferromagnetically. Ferrimagnetic insulators, such as ferrites and garnets, have been employed for microwave<sup>2</sup> and spin-wave<sup>3</sup> applications because of their low magnetic damping (and thus low energy dissipation and narrow resonant linewidth). Another traditional application area of ferrimagnets is magneto-optical recording<sup>4–6</sup>, in which magnetic information is recorded by laser illumination, which increases the local temperature to close to the Curie temperature, combined with a small applied magnetic field that induces the magnetization reversal. For this thermomagnetic recording, rare earth–transition metal (RE–TM) ferrimagnetic alloys, such as GdFeCo and TbCo, have exhibited excellent performances, enabled by the tunability of their compensation temperatures to achieve a high stability near room temperature as well as a large perpendicular anisotropy field even in thick films<sup>7</sup>, which is difficult to achieve with ferromagnets. These traditional applications have treated ferrimagnets as essentially low-magnetization ferromagnets, but ignored the antiferromagnet-like nature of the microscopic exchange interaction, even though the small net magnetization originates from the antiferromagnet-like coupling, as noticed in the original work<sup>1</sup>.

Recent studies highlighted that compensated ferrimagnets, which consist of inequivalent sublattices, combine the advantages of both antiferromagnets and ferromagnets that had previously been largely considered mutually exclusive. The advantages stem from two intrinsic properties of ferrimagnets. First, the antiparallel alignment of sublattice moments allows one to investigate antiferromagnetic spin dynamics and transport, currently a subject of extensive research in antiferromagnetic spintronics<sup>8,9</sup>. Second, ferrimagnets, such as RE–TM compounds, consist of inequivalent magnetic atoms that have distinct magnetic, electronic and/or optical properties, and thereby offer a sublattice-specific control and/or address coupled sublattice dynamics (Fig. 1b). This inequivalence, together with the antiferromagnetic sublattice coupling, is responsible for

the all-optical switching (AOS) of magnetization in ferrimagnetic GdFeCo by a single femtosecond laser pulse<sup>10–14</sup>. It also allows ferrimagnets to have finite Zeeman coupling and spin polarization, both of which are absent in antiferromagnets. The Zeeman coupling allows one to control ferrimagnets with an external magnetic field, which is crucial to create spin textures such as domain walls (DWs) and skyrmions. The finite spin polarization enables one to polarize and detect spin currents, which is crucial for research on current-induced ferrimagnetic dynamics. The inequivalence combined with the antiferromagnet-like coupling also results in a great tunability of their net magnetization  $M$  and angular momentum density  $A$  (Fig. 1c). In ferromagnets, the gyromagnetic ratio  $\gamma$  ( $= M/A$ ) is almost independent of temperature. In antiferromagnets, both  $M$  and  $A$  vanish in equilibrium due to the perfect cancellation between neighbouring atoms. In ferrimagnets, on the contrary, the two quantities can be manipulated almost independently by varying the temperature and/or composition, which expands the potential of the magnetic properties greatly. The dashed line in Fig. 1c represents an accessible trajectory of  $M$  and  $A$  by varying the temperature and/or composition. The trajectory passes two special points: the angular momentum compensation point  $T_A$ , at which the net angular momentum vanishes, and the magnetization compensation point  $T_M$ , at which the net magnetization vanishes. In particular,  $T_A$  is special from the viewpoint of combining ferromagnetic and antiferromagnetic features, because antiferromagnetic magnetization dynamics is realized, but Zeeman coupling is finite at this compensation point. In this respect, ferrimagnets can serve as a material platform not only to investigate antiferromagnetic spin textures and dynamics but also to realize practical spintronic devices that exploit the advantages of both antiferromagnets and ferromagnets.

In this Review, we discuss the most remarkable studies on ferrimagnets concerning both spin dynamics and spin transport, with a particular focus on the important roles of individual sublattices and antiferromagnet-like coupling between them. With respect to spin dynamics, we describe ultrafast longitudinal ferrimagnetic spin dynamics on femto- to picosecond timescales and transversal dynamics on longer timescales in an antiferromagnetically coupled

<sup>1</sup>Department of Physics, Korea Advanced Institute of Science and Technology (KAIST), Daejeon, Korea. <sup>2</sup>Department of Materials Science and Engineering, Massachusetts Institute of Technology, Cambridge, MA, USA. <sup>3</sup>Department of Materials Science and Engineering, Korea University, Seoul, Korea. <sup>4</sup>KU-KIST Graduate School of Converging Science and Technology, Korea University, Seoul, Korea. <sup>5</sup>Institute of Chemical Research, Kyoto University, Kyoto, Japan. <sup>6</sup>Center for Spintronics Research Network (CSR/N), Graduate School of Engineering Science, Osaka University, Osaka, Japan. <sup>7</sup>Institute for Molecules and Materials, Radboud University, Nijmegen, the Netherlands. <sup>8</sup>State Key Laboratory of Advanced Technology for Materials Synthesis and Processing, Wuhan University of Technology, Wuhan, China. <sup>9</sup>Department of Electrical and Computer Engineering, National University of Singapore, Singapore, Singapore. ✉e-mail: [kjlee@kaist.ac.kr](mailto:kjlee@kaist.ac.kr)

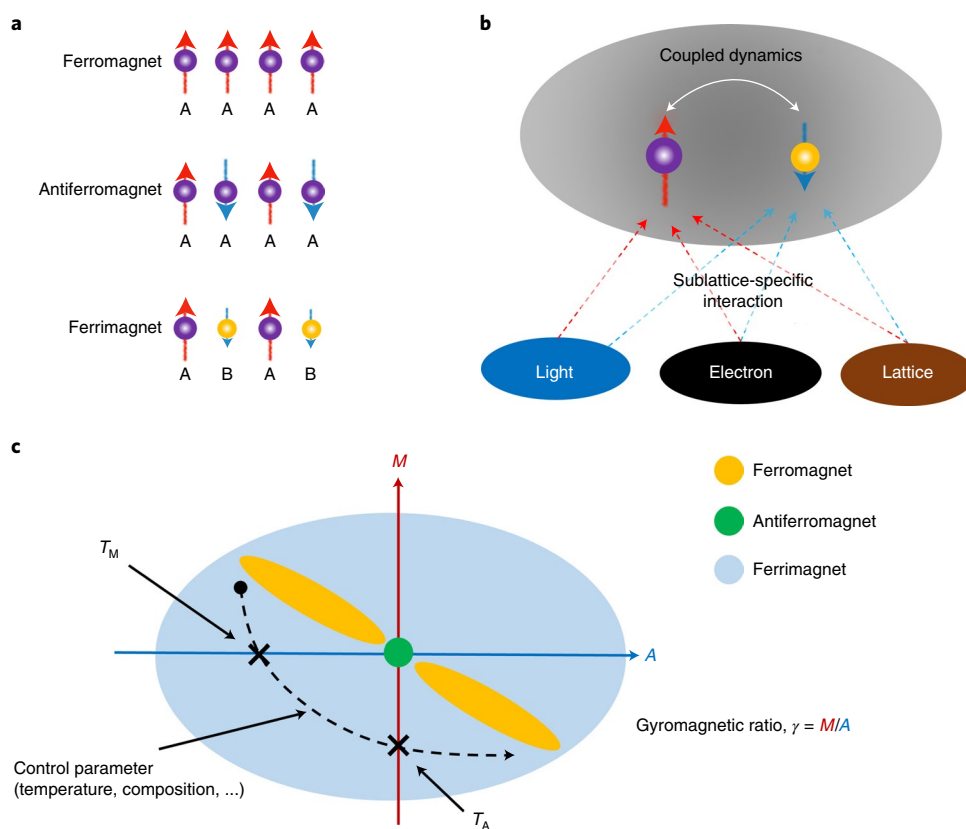


**Fig. 1 | Different classes of long-range magnetic order.** **a**, Alignment of magnetic moments in three types of magnets. Ferromagnets and antiferromagnets consist of only one type of magnetic atoms, whereas ferrimagnets consist of two (or more) inequivalent magnetic atoms, denoted by A and B. **b**, A schematic illustration of the antiferromagnetically coupled dynamics of two sublattices and sublattice-specific interactions with light, an electron and a lattice. **c**, A schematic phase diagram of magnets as a function of the magnetization  $M$  and the angular momentum density  $A$ . The colours shown span the range of accessible parameters for each class of magnetic order. Ferrimagnets have a much wider and greater tunability than ferromagnets and antiferromagnets.

two-sublattice system. We note that both longitudinal and transversal dynamics must be taken into account at the same time in general. However, the distinction between longitudinal and transversal dynamics is a reasonable approximation owing to their very different timescales. We further elaborate on the longitudinal dynamics in combination with the AOS<sup>10–16</sup> and ultrafast demagnetization<sup>17,18</sup>. We also elaborate on the transversal dynamics in connection with fast DW dynamics<sup>19–25</sup> and the vanishing skyrmion Hall effect<sup>26,27</sup> at  $T_A$ , which are reasonably described by a theory based on staggered spin order<sup>26,28,29</sup>. For spin transport, the antiferromagnetic alignment of atomic spins results in a long spin coherence length for transverse spin currents<sup>30,31</sup> and an enhanced non-adiabatic spin torque on ferrimagnetic DWs<sup>32</sup>. These intriguing features of ferrimagnets highlight their potential as an enabling material platform for spintronic applications, which has so far been dominated mostly by ferromagnets, whereas antiferromagnets have only been considered more recently<sup>8,9</sup>.

### Longitudinal spin dynamics and all-optical switching

Femtosecond laser excitation of magnetically ordered materials can lead to ultrafast, meaning subpicosecond, demagnetization, described by the longitudinal spin dynamics in which the magnitudes of magnetic moments are not conserved<sup>17</sup>. The ultrafast demagnetization was described within a phenomenological three-temperature model<sup>17</sup>, in which laser energy is first absorbed by electrons, which leads to an ultrafast, instantaneous (on the timescale of the laser pulse) excitation of the electrons. Subsequently,

energy and angular momentum are exchanged among the electron, phonon and spin reservoirs, described by electron–phonon and spin–lattice relaxation parameters.

Various mechanisms for angular momentum transfer to the surroundings have been discussed, from phenomenological descriptions<sup>33</sup> to first-principles calculations<sup>34</sup>. The demagnetization rates were found to scale inversely with the magnetic moment and to relate to the spin–lattice coupling<sup>35–37</sup>. In multisublattice systems, this demagnetization rate is also affected by the sign of the sublattice exchange<sup>38</sup>. This means that the same moment can have different demagnetization rates, depending on whether it is coupled ferromagnetically or antiferromagnetically to another moment, as confirmed experimentally<sup>37</sup>. As shown below, this can lead to AOS in ferrimagnets with distinct sublattices, such as in RE–TM alloys.

Before moving to the AOS, we briefly introduce some distinct features of the electronic band structures of RE–TM ferrimagnets that determine their unique properties. Ferrimagnets and antiferromagnets are different on this level, as the electron bands in antiferromagnets exhibit the Kramers degeneracy, which is not the case for ferrimagnets. In this respect, ferrimagnets are similar to ferromagnets, but there are important differences. In RE–TM ferrimagnets, the  $5d$  RE electrons have an important role in the antiferromagnetic RE–TM coupling in equilibrium<sup>39,40</sup>. The RE  $4f$  spins, the band of which lies far below the Fermi level<sup>41</sup>, create positive local  $5d$  moments (in the same RE atom) through an intra-atomic  $4f$ – $5d$  exchange. These RE  $5d$  spins couple antiferromagnetically to the TM  $3d$  spins through an interatomic exchange, because the RE  $5d$

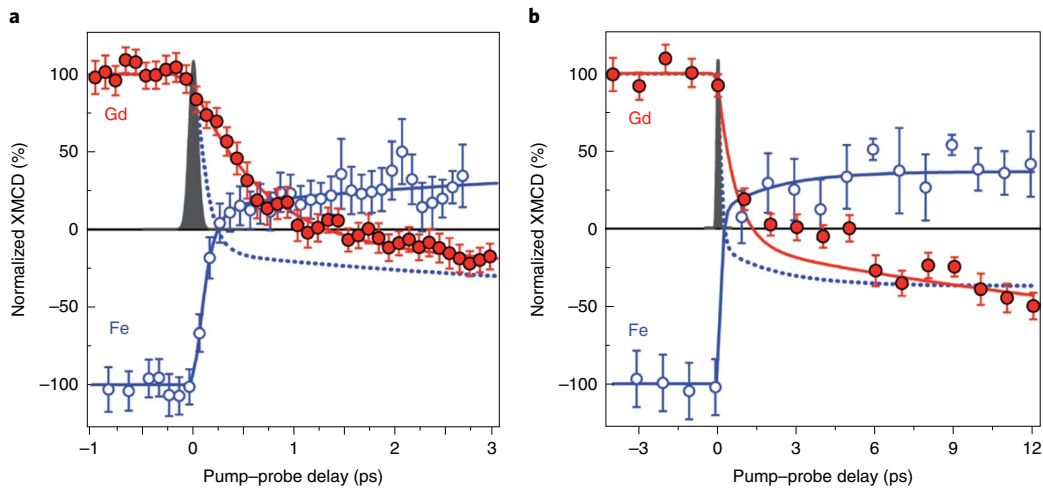


**Fig. 2 | All-optical magnetization switching of GdFeCo with linearly polarized light. a, b,** Transient dynamics of Fe and Gd magnetic moments within the first 3 ps (**a**) and within a 12 ps timescale (**b**). Element-resolved dynamics of the Fe (open circles) and Gd (filled circles) magnetic moments of GdFeCo on pumping with a linearly polarized femtosecond laser pulse were measured by time-resolved X-ray magnetic circular dichroism (XMCD). Error bars represent the statistical standard error. Figure reproduced with permission from ref. <sup>11</sup>, Springer Nature Ltd.

orbitals (for example, Gd and Tb) are below half-filled, whereas the TM  $3d$  orbitals (for example, Co, Fe and Ni) are above half-filled<sup>39</sup>. These features are responsible for the unique optical and electrical responses of RE–TM ferrimagnets. Concerning the optical response, a laser pulse mostly excites TM  $3d$  and RE  $5d$  spins, not RE  $4f$  spins, and the ultrafast demagnetization of the TM  $3d$  spins is channelled to the RE  $4f$  ones by the small intermediate RE  $5d$  spins. This is an additional reason for the slower demagnetization of RE  $4f$  moments. Moreover, the antiferromagnetic alignment between RE  $5d$  and TM  $3d$  spins at the Fermi level allows non-equilibrium conduction electron spins to move through an effective antiferromagnetic order, which corresponds to exchange fields with different magnitudes and alternating signs on the atomic scale.

One of the most remarkable experimental findings in ferrimagnets was the ultrafast AOS at zero applied magnetic field in GdFeCo, which used a single 40 fs circularly polarized laser pulse. The strong laser pulse excited the electrons to extremely non-equilibrium and susceptible states within a few hundred femtoseconds. The helicity of the light appeared to determine the direction of the subsequent magnetization of the cooled equilibrium state, and thereby realized a deterministic AOS. At that time, it was a common belief that a circular polarization of light was essential for deterministic AOS because it broke the time-reversal symmetry.

However, a surprising discovery that refuted this common belief was made: the deterministic AOS of GdFeCo was achieved with a linearly polarized femtosecond laser pulse<sup>11</sup>. Obtaining the physical picture for this AOS required separately probing the ultrafast dynamics of individual magnetic sublattices (Gd and Fe) via the element-specific technique of X-ray magnetic circular dichroism. First, pumping with a linearly polarized 60 fs laser pulse gave rise to an ultrafast excitation of GdFeCo, which decreased the magnetizations of both sublattices rapidly, but differently. Although the Fe magnetization collapsed within 0.2 ps, the Gd demagnetization took as long as 1.5 ps (Fig. 2a,b). The difference in the demagnetization timescales of the two sublattices is remarkable given the strong antiferromagnetic exchange interaction between them, but it can be understood from the fact that the Gd moment, the main contribution of which comes from the  $4f$  spins, is about four times larger than that of Fe. Subsequently, after the electronic bath cooled down, the antiferromagnetic exchange interaction between the two sublattices became effective and the continuing slow demagnetization of Gd was accompanied by the growth of the Fe moment in the

opposite direction, which thus conserved the total angular momentum. This resulted in the observed transient ferromagnetic-like state with parallel Fe and Gd magnetizations in the time interval between 0.2 ps and 1.5 ps after the excitation. Finally, after the complete demagnetization of the Gd sublattice in the presence of a finite reversed Fe magnetization, the antiferromagnetic exchange interaction drove the Gd sublattice in the antiparallel direction of the Fe magnetization on a longer timescale, which completed the AOS of GdFeCo with a linearly polarized laser pulse. This result emphasizes the important role of distinct sublattices in the AOS with linearly polarized light. Note that the aforementioned mechanism for AOS is inoperative for antiferromagnets that consist of identical magnetic atoms.

Based on the Onsager relations for spin dynamics<sup>42,43</sup>, the equations of motion for a system of two inequivalent collinear sublattices A and B have been derived as<sup>12</sup>:

$$\frac{\partial S_A}{\partial t} = \lambda_e (H_A - H_B) + \lambda_A H_A, \quad (1)$$

$$\frac{\partial S_B}{\partial t} = \lambda_e (H_B - H_A) + \lambda_B H_B, \quad (2)$$

where  $S_{A,B}$  denotes the macroscopic angular momenta of the sublattices A, B and is related to the magnetization  $m_{A,B}$  by  $S_{A,B} = m_{A,B}/\gamma_{A,B}$ ,  $\lambda_e$  describes the transfer of angular momentum between the two sublattices,  $\lambda_{A,B}$  describes the transfer of angular momentum between the sublattices and the environment (and thus the damping of longitudinal spins) and the effective field  $H_{A,B}$  is derived from the magnetic energy, which includes the exchange energy. This simple model describes the observed non-equilibrium dynamics reasonably in terms of an ultrafast heating mechanism that affects the magnitude of the magnetization and the exchange interaction between the sublattices, which transfers angular momentum between them. The transversal dynamics is ignored here<sup>12</sup> as it takes place at much longer timescales, but it is, of course, important for the relaxation to equilibrium at longer times<sup>44</sup>. Moreover, these results are completely consistent with the atomistic simulations of a large ensemble of spins<sup>14</sup>, in which the spin dynamics is described by the transversal dynamics of individual spins in their local exchange fields via the Landau–Lifshitz–Gilbert (LLG) equations. When summing over multiple atomic spins, this results in a macroscopic demagnetization

and thus longitudinal macroscopic dynamics. This approach is now generally accepted in the community<sup>45–47</sup>. A similar picture was derived for synthetic ferrimagnets<sup>15</sup>, which was, indeed, observed experimentally<sup>48,49</sup>. It was also shown that the observed helicity dependence in GdFeCo<sup>10</sup> could be contributed to magnetic circular dichroism<sup>50</sup>, that is, the light absorption depends on the helicity of the light, consistent with the ultrafast heating mechanism. We note that for all these cases of deterministic AOS with a single linearly polarized laser pulse, a subsequent pulse will bring the system back to its previous state (toggle switching).

Recently, all these results were generalized, which resulted in a phase diagram that describes different pathways for AOS. It implies that, for proper pulse and sample parameters (pulse width, fluence and sample composition), a femtosecond or even picosecond excitation pulse can reverse the original magnetization, independent of the polarization of the pulse<sup>13</sup>. Given the different demagnetization times  $\tau_{A,B}$  of sublattices A and B, the laser pulse width  $\tau_1$  must be in an appropriate window for a successful AOS. Exciting such a system adiabatically (that is,  $\tau_1 > \tau_{s-l}$ , where  $\tau_{s-l}$  is the spin–lattice relaxation time) will lead to the complete demagnetization of both sublattices simultaneously, with no reversal. However, when  $\tau_1 < \tau_{A,B} < \tau_{s-l}$ , the difference in the demagnetization rates of A and B becomes effective and the switching is achieved through the different longitudinal spin dynamics of  $m_A$  and  $m_B$ , that is,  $m_A$  reaches zero before  $m_B$  does. This works even for picosecond laser pulses, as long as the non-adiabatic condition,  $\tau_1 < \tau_{A,B} < \tau_{s-l}$ , is fulfilled<sup>51,52</sup>. In the time window between  $\tau_A$  and  $\tau_B$ , the experimentally observed transient ferromagnetic state is formed, with the already reversing  $m_A$  pointing in the same direction as the still decreasing  $m_B$ . However, the polarity of this transient state depends on the concentration of B (ref. <sup>51</sup>). It was shown<sup>13</sup> that when  $m_B$  reaches zero before  $m_A$ , no switching can be achieved.

As one of the key ingredients for AOS is a non-adiabatic excitation of the electronic subsystem, not only optical stimuli but also other triggers (such as a short current pulse) can be used<sup>53</sup>. As the excitation only involves the transfer of optical energy to the electron subsystem, the specific photon energy is not relevant, which was confirmed by changing the latter with a factor of more than 20, with the AOS still seen as long as the pulse width was in the right regime<sup>13</sup>. Single-shot switching has so far been observed in a limited number of RE–TM systems other than GdFeCo, such as the TbFeCo alloy<sup>54</sup> and Gd/Co<sup>48</sup> and Tb/Co<sup>49</sup> multilayers. However, it was also recently achieved in the ferrimagnetic Heusler alloy Mn<sub>2</sub>Ru<sub>x</sub>Ga without RE elements<sup>55</sup>, which could be described by the same exchange-driven mechanism<sup>56</sup>. Single-shot switching was also observed in a ferrimagnetic garnet<sup>57</sup>, but in that case, the mechanism relied on an optically induced change of the magnetic anisotropy.

We also note that the timescale in which a material goes back to its equilibrium limits the writing speed of AOS. A recent work demonstrated a rewriting time of 300 ps, but also discussed the routes for further optimization<sup>58</sup>, whereas another work showed that nanoscale fabrication considerably decreases the switching times<sup>59</sup>.

### Transversal spin dynamics and motion of spin texture

In this section, we describe the transversal spin dynamics of a two-sublattice ferrimagnet in which the magnitudes of magnetic moments  $\mathbf{m}_A$  and  $\mathbf{m}_B$  are conserved and they are coupled by anti-ferromagnetic exchange. Low-energy transversal dynamics of (col-linear) ferrimagnets can be described by the staggered order  $\mathbf{n}$  ( $= (\mathbf{m}_A - \mathbf{m}_B)/2$ ) with unit length. The equation of motion for  $\mathbf{n}$  can be written as<sup>19,28,29,60–62</sup>:

$$\delta_s \dot{\mathbf{n}} - \rho \mathbf{n} \times \ddot{\mathbf{n}} - \alpha s \mathbf{n} \times \dot{\mathbf{n}} = -\mathbf{n} \times \mathbf{f}_{\text{eff}} + \tau_{\text{STT}} + \tau_{\text{SOT}}, \quad (3)$$

where  $\dot{\mathbf{n}} = \partial \mathbf{n} / \partial t$ ,  $\ddot{\mathbf{n}} = \partial^2 \mathbf{n} / \partial t^2$ ,  $\delta_s$  is the net angular momentum density,  $\alpha$  ( $> 0$ ) is the Gilbert damping,  $s$  is the sum of angular momentum

densities of the two sublattices,  $\rho$  is the inertia associated with anti-ferromagnetic dynamics of  $\mathbf{n}$ ,  $\mathbf{f}_{\text{eff}} \equiv -\delta U / \delta \mathbf{n}$  is the effective energy conjugate to  $\mathbf{n}$ , and  $U[\mathbf{n}]$  is the potential energy, which includes the Zeeman term  $-M_i \mathbf{n} \cdot \mathbf{H}$  in an external field  $\mathbf{H}$ , where  $M_i$  is the net magnetization. See Box 1 for the detailed definition of each parameter and the derivation of equation (3) from the coupled LLG equations of two sublattices. The last two terms on the right-hand side are the spin-transfer torque (STT)<sup>32</sup> and the spin-orbit torque (SOT)<sup>20,21,29</sup>.

Equation (3) describes two fundamental spin-wave modes in ferrimagnets<sup>63–65</sup>: the ferromagnetic-like low-frequency precession mode and the antiferromagnetic-like high-frequency exchange mode. It also interpolates between ferromagnetic and antiferromagnetic dynamics. First,  $\delta_s$  vanishes at  $T_A$ , and thus equation (3) is reduced to that of antiferromagnets. One crucial difference is that the net magnetization  $M_i$  is finite in ferrimagnets at  $T_A$ , whereas it is zero in antiferromagnets. This gives rise to one of the unique properties of ferrimagnets at  $T_A$ : they offer antiferromagnet-like spin dynamics, yet the dynamics can be controlled by an external field as in ferromagnets. Second, far away from  $T_A$ , where  $\delta_s$  is sufficiently large, the  $\rho \mathbf{n} \times \ddot{\mathbf{n}}$  term in equation (3) can be ignored so that it reduces to that of ferromagnets.

For metallic ferrimagnets, magnetization dynamics can be induced by STT, which consists of adiabatic and non-adiabatic terms<sup>32</sup>:  $\tau_{\text{STT}} = P(\mathbf{J} \cdot \nabla) \mathbf{n} - \beta P \mathbf{n} \times (\mathbf{J} \cdot \nabla) \mathbf{n}$ , where  $\mathbf{J}$  is the charge-current density,  $P$  is the spin polarization and  $\beta$  is the non-adiabaticity. In RE–TM ferrimagnets,  $P$  is finite even at  $T_A$  because of unequal contributions from the two sublattices. This is another unique difference between ferrimagnets and antiferromagnets: ferrimagnets at  $T_A$  offer antiferromagnet-like dynamics driven by the adiabatic STT, which is not possible with antiferromagnets for which  $P$  averaged over two sublattices is zero.

The aforementioned features of ferrimagnets at  $T_A$  are manifested vividly in the DW dynamics. To see this, we describe the ferrimagnetic DW dynamics based on the collective coordinate approach with two dynamic variables, the DW position  $X$  and the DW angle  $\Phi$ . In ferromagnets, these conjugate variables are gyrotropically coupled by the spin Berry phase proportional to  $\delta_s$ : the force on  $X$  induces the dynamics of  $\Phi$  and vice versa. This gyrotropic coupling forces DW translation to be accompanied by DW precession, which leads to severely slowing down the DW translational motion, known as the Walker breakdown<sup>66–68</sup>. In antiferromagnets, however, the dynamics of  $X$  and  $\Phi$  are decoupled because  $\delta_s = 0$ . The DW dynamics in antiferromagnets is thus free from the Walker breakdown and can be much faster than that in ferromagnets<sup>69,70</sup>.

In the presence of an easy-axis external field  $\mathbf{H} = H\hat{z}$  larger than the Walker threshold, the steady-state velocity  $\langle \dot{X} \rangle = V$  and angular velocity  $\langle \dot{\Phi} \rangle = \Omega$  are given by<sup>19</sup>:

$$V = \frac{\alpha s \lambda M_i H}{\delta_s^2 + (\alpha s)^2}, \quad \Omega = \frac{\delta_s M_i H}{\delta_s^2 + (\alpha s)^2}, \quad (4)$$

where  $\lambda$  is the DW width. Note that  $\Omega$  vanishes at  $T_A$  ( $\delta_s = 0$ ) where the antiferromagnetic DW dynamics is realized and  $V$  is maximum. This can be understood from the energy consumption. The energy dissipation rate caused by the dynamics of  $X$  and  $\Phi$  is proportional to  $\alpha s(V^2 + \lambda^2 \Omega^2) / \lambda$  (ref. <sup>19</sup>). For a given energy dissipation rate, the DW should move the fastest when all the energy is used to move it with no energy leakage to the DW precession (Fig. 3a–e).

For STT-driven motion, the DW velocity is given by<sup>32</sup>:

$$V = -\frac{\delta_s P J}{\delta_s^2 + (\alpha s)^2} - \frac{\alpha s \beta P J}{\delta_s^2 + (\alpha s)^2}. \quad (5)$$

Here, the first and the second terms describe the contributions of adiabatic and non-adiabatic STTs, respectively. Note that, at

**Box 1 | The equation of motion for ferrimagnets**

Here we present a way to derive equation (3) from the coupled LLG equations for two inequivalent sublattices with unit magnetization vectors  $\mathbf{m}_A$  and  $\mathbf{m}_B$ , following a procedure applied for antiferromagnets<sup>132</sup>. Here we ignore spin-torque terms for simplicity. We consider the following simple discrete Hamiltonian for one-dimensional ferrimagnets:

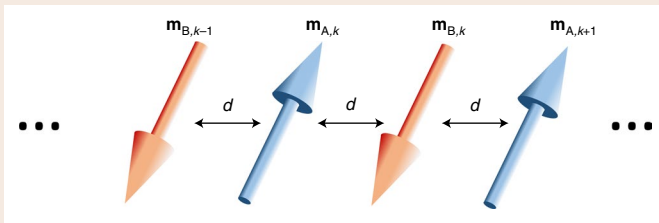
$$H = J_{\text{ex}} \sum_k (\mathbf{m}_{A,k} \cdot \mathbf{m}_{B,k} + \mathbf{m}_{B,k} \cdot \mathbf{m}_{A,k+1}) - K_0 \sum_k [(\mathbf{m}_{A,k} \cdot \mathbf{z})^2 + (\mathbf{m}_{B,k} \cdot \mathbf{z})^2] - \mathbf{H} \cdot \sum_k (\mu_A \mathbf{m}_{A,k} + \mu_B \mathbf{m}_{B,k}), \quad (7)$$

where  $J_{\text{ex}} > 0$  is the antiferromagnetic exchange constant,  $K_0$  the uniaxial anisotropy constant,  $\mathbf{H}$  an external magnetic field and  $\mu_{A,B}$  the magnetic moments. The LLG equation for the sublattice  $i$  ( $i = A, B$ ) is given by:

$$\mathbf{N}_i = s_i \dot{\mathbf{m}}_i + M_i \mathbf{m}_i \times \mathbf{H}_{\text{eff},i} - \alpha_i s_i \mathbf{m}_i \times \dot{\mathbf{m}}_i = 0, \quad (8)$$

where  $s_i = M_i/\gamma_i$  is the angular momentum density,  $M_i = \mu_i/2d^3$  is the saturation magnetization,  $\gamma_i$  is the gyromagnetic ratio,  $\dot{\mathbf{m}}_i = \partial \mathbf{m}_i / \partial t$ ,  $\mathbf{H}_{\text{eff},i} = -\delta U / (M_i \delta \mathbf{m}_i)$  is the effective field conjugate to  $\mathbf{m}_i$  and  $\alpha_i$  is the damping constant. For simplicity, we assume  $\alpha_A = \alpha_B = \alpha$ . The effective fields  $\mathbf{H}_{\text{eff},i}$  for the sublattices obtained with the energy  $U$  in the continuum limit are given by:

$$\mathbf{H}_{\text{eff},A} = -\frac{A_x}{M_A} \mathbf{m}_B - \frac{A_{\text{ex}}}{2M_A} \mathbf{m}''_B + \frac{K}{2M_A} (\mathbf{m}_A \cdot \hat{\mathbf{z}}) \hat{\mathbf{z}} + \mathbf{H}, \quad (9)$$



Schematic illustration of the magnetizations  $\mathbf{m}_A$  and  $\mathbf{m}_B$  of the two sublattices, where  $d$  is the intersublattice distance.

$T_A$  ( $\delta_s = 0$ ), the adiabatic STT does not contribute to DW motion, whereas the non-adiabatic STT moves the DW. These behaviours are consistent with theories for antiferromagnetic DWs<sup>71</sup>. We note that the non-adiabatic effective field is staggered, which means that the non-adiabatic STT induces opposite effective magnetic fields on two sublattices, and thus linearly couples to the staggered order. In contrast, the non-adiabatic STT for ferromagnetic DWs is an effective uniform magnetic field that linearly couples to the local magnetization. Equation (5) also shows that the adiabatic contribution is antisymmetric with respect to  $\delta_s = 0$ , whereas the non-adiabatic contribution is symmetric. This distinct symmetry helps to decompose the adiabatic and non-adiabatic contributions from the measured DW speed<sup>32</sup>.

The above discussion shows that the ferrimagnetic DW velocity is maximum at  $T_A$  when it is driven by an effective field (either an external magnetic field or a non-adiabatic torque). Recent works show that the SOT-driven ferrimagnetic DW speed is also maximum at  $T_A$  because the SOT serves as an effective field<sup>20,21,29</sup>. Therefore, the fastest DW motion at  $T_A$  is a general phenomenon, regardless of the type of driving mechanism.

$$\mathbf{H}_{\text{eff},B} = -\frac{A_x}{M_B} \mathbf{m}_A - \frac{A_{\text{ex}}}{2M_B} \mathbf{m}''_A + \frac{K}{2M_B} (\mathbf{m}_B \cdot \hat{\mathbf{z}}) \hat{\mathbf{z}} + \mathbf{H}, \quad (10)$$

where  $A_x = J_{\text{ex}}/d^3$ ,  $A_{\text{ex}} = J_{\text{ex}}/d$ ,  $\mathbf{m}''_i = \partial^2 \mathbf{m}_i / \partial x^2$  and  $K = 2K_0/d^3$ . Here, the third term represents the anisotropy field, for example,  $\mathbf{H}_{\text{ani},A} = K (\mathbf{m}_A \cdot \hat{\mathbf{z}}) \hat{\mathbf{z}} / 2M_A$ .

We introduce the Néel order vector  $\mathbf{n} = \frac{\mathbf{m}_A - \mathbf{m}_B}{2}$  and the total magnetization vector  $\mathbf{m} = \mathbf{m}_A + \mathbf{m}_B$ , which are orthogonal to each other. For a strong exchange,  $|\mathbf{n}| \approx 1 \gg |\mathbf{m}|$  is satisfied. Introducing  $s$  ( $= s_A + s_B$ ) and  $\delta_s$  ( $= s_A - s_B$ ), and expanding  $\mathbf{N}_A + \mathbf{N}_B$  and  $\mathbf{N}_A - \mathbf{N}_B$  up to the second order in the derivatives,  $\mathbf{m}$ ,  $\alpha$  and  $\delta_s$ , and working to the first order in the anisotropy and external fields gives:

$$\delta_s \dot{\mathbf{n}} + \frac{s}{2} \dot{\mathbf{m}} - \alpha s \mathbf{n} \times \dot{\mathbf{n}} + A_{\text{ex}} \mathbf{n} \times \mathbf{n}'' + M_I \mathbf{n} \times \mathbf{H} + K n_z \mathbf{n} \times \hat{\mathbf{z}} = 0, \quad (11)$$

$$s \dot{\mathbf{n}} + 2A_x \mathbf{m} \times \mathbf{n} + M_I \mathbf{n} \times \mathbf{H} = 0 \quad (12)$$

where  $M_i = M_A - M_B$  and  $M_I = M_A + M_B$ . From equation (12),  $\mathbf{m}$  can be expressed in terms of  $\mathbf{n}$  and  $\mathbf{H}$ :

$$\mathbf{m} = \frac{s}{2A_x} \dot{\mathbf{n}} \times \mathbf{n} - \frac{M_I}{2A_x} [\mathbf{n} (\mathbf{n} \cdot \mathbf{H}) - \mathbf{H}]. \quad (13)$$

By integrating out  $\mathbf{m}$  and its time derivative from equation (11) based on equation (13) and applying the same order counting described above, we obtain:

$$\delta_s \dot{\mathbf{n}} - \rho \mathbf{n} \times \ddot{\mathbf{n}} - \alpha s \mathbf{n} \times \dot{\mathbf{n}} = \mathbf{f}_{\text{eff}} \times \mathbf{n}, \quad (14)$$

where  $\rho$  ( $= s^2/4A_x = s^2 d^3/4J_{\text{ex}}$ ) is the inertia associated with the antiferromagnetic dynamics of  $\mathbf{n}$  and  $\mathbf{f}_{\text{eff}}$  ( $= A_{\text{ex}} \mathbf{n}'' + M_I \mathbf{H} + K (\mathbf{n} \cdot \hat{\mathbf{z}}) \hat{\mathbf{z}}$ ) is the effective energy conjugate to  $\mathbf{n}$ . Note that equation (14) is equivalent to equation (3) except for the spin-torque terms, when the energy functional  $U = \int dV [A_{\text{ex}} (\mathbf{n}')^2/2 - K n_z^2/2 - M_I \mathbf{H} \cdot \mathbf{n}]$  is used. Finally, we note that numerical factors in the parameters depend on the dimensionality and the number of moments considered.

The great tunability of ferrimagnetic dynamics is manifested also in the dynamics of magnetic skyrmions<sup>72-74</sup>, swirling spin textures stabilized by the Dzyaloshinskii–Moriya interaction<sup>75,76</sup>. Ferromagnetic skyrmions were intensively studied owing to their robustness associated with topological characteristics and their potential utility as point-like information carriers<sup>54,77-83</sup>. However, it turned out that ferromagnetic skyrmions exhibit several features that must be overcome for applications. First, stray fields, helpful for room-temperature stability, tend to increase the skyrmion size<sup>20,84</sup>, which leads to bubble-like structures that are typically 100 nm or larger<sup>78-83</sup>. Second, ferromagnetic skyrmions exhibit the so-called skyrmion Hall effect (like the ordinary Hall effect of a charged particle in the presence of a magnetic field), which leads to skyrmion motion at a skew angle, known as the skyrmion Hall angle  $\theta_{\text{skH}}$ , from the driving current direction<sup>85,86</sup>. The skyrmion Hall effect arises from a Magnus-like force, rooted in the gyrotropic coupling, which is proportional to  $\delta_s$ . It was predicted<sup>87,88</sup> that the skyrmion Hall effect vanishes for antiferromagnetic skyrmions due to a vanishing  $\delta_s$ . Ferrimagnetic skyrmions can realize this Hall-effect-free motion at  $T_A$  ( $\delta_s = 0$ ). The skyrmion Hall angle  $\theta_{\text{skH}}$  is determined by balancing

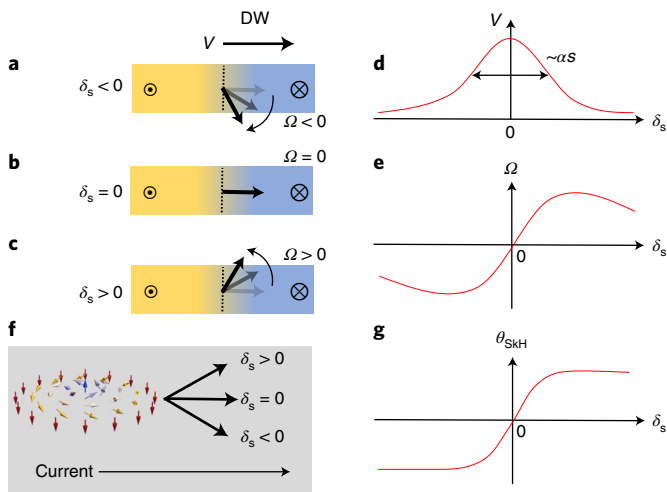


**Fig. 3 | DW and skyrmion motion in ferrimagnets.** **a–c**, Schematic illustration of DW motion at the velocity  $V$  driven by an external field applied along the out-of-plane direction. The finite velocity of the DW driven by the field gives rise to the DW precession velocity  $\Omega \propto \delta_s V$  via the gyrotropic coupling proportional to the net angular momentum density  $\delta_s$  ( $<0$  (**a**),  $=0$  (**b**) and  $>0$  (**c**)). Therefore, the angular velocity  $\Omega$  is zero at the angular momentum compensation point with  $\delta_s = 0$  (**b**). **d**, The DW velocity as a function of the net angular momentum density, which shows a maximum at  $\delta_s = 0$  (where the translational motion and the angular motion are decoupled, as in antiferromagnets) and decreases away from it. The width of the curve is on the order of  $\alpha s$ . **e**, The DW precession frequency as a function of the net angular momentum density. **f**, Schematic illustration of a skyrmion driven by a current via SOT. Its motion is deflected from the current direction by the Magnus-like force when the net angular momentum density is finite, and exhibits the skyrmion Hall effect, whereas it is parallel to the current, as predicted for antiferromagnetic skyrmions, when the net angular momentum density is zero. **g**, The skyrmion Hall angle  $\theta_{\text{skH}}$ , which is the angle of the skyrmion motion with respect to the current direction as a function of the net angular momentum density.

the Magnus force,  $\propto \delta_s Q$ , and the viscous force,  $\propto \alpha s$ , where  $Q$  is the skyrmion number that measures how many times the staggered magnetization  $\mathbf{n}(\mathbf{r})$  wraps the unit sphere<sup>26,27</sup>. For SOT-induced skyrmion motion in ferrimagnets,  $\theta_{\text{skH}}$  is given by<sup>27</sup>:

$$\theta_{\text{skH}} = \tan^{-1} \left( \frac{4\pi\delta_s Q}{\alpha s D} \right), \quad (6)$$

where  $D$  is a dimensionless number determined by the skyrmion profile. At  $T_A$ , where  $\delta_s = 0$ ,  $\theta_{\text{skH}}$  is zero as for antiferromagnetic skyrmions. The sign and magnitude of  $\theta_{\text{skH}}$  can be manipulated by changing the temperature or composition, which demonstrates a great tunability of skyrmion dynamics in ferrimagnets (Fig. 3f,g).

Experiments on the dynamics of DWs and skyrmions in ferrimagnets have realized many of the behaviours described above in the vicinity of  $T_A$ . We start with the DW motion. Using GdFeCo with a perpendicular magnetic anisotropy (Fig. 4a)<sup>19</sup>, it was shown that the field-driven DW velocity exhibits a maximum at around  $T \approx 310$  K, regardless of the applied field, and it decays as the temperature moves away from this critical point. According to equation (4), this critical temperature is  $T_A$ , also supported by numerical modelling<sup>19</sup>. Therefore, the field-driven DW motion allows for the experimental determination of  $T_A$ , which has been challenging owing to the absence of a direct experimental probe of  $\delta_s$ .

The SOT can also move a ferrimagnetic DW quickly in the vicinity of  $T_A$ . Figure 4b shows the velocity of SOT-driven DWs in

GdCo at various temperatures<sup>20</sup>. The velocity attains a maximum at  $T \approx 260$  K, which is identified as  $T_A$ . There is one important difference between the field-driven case and the SOT-driven case: SOT can drive the DW at all temperatures, which include  $T_M$  at which the net magnetic moment vanishes and thus the field-driven motion is infeasible. Not only is the temperature a control parameter of  $\delta_s$ , but so is the composition of the ferrimagnets. It was experimentally demonstrated<sup>24</sup> that a DW is driven by SOT in  $\text{Gd}_x\text{Co}_{1-x}$  samples, in which the DW velocity exhibits a maximum at the Gd composition  $x \approx 0.23$ , which corresponds to the angular momentum compensation. The maximum velocity reported in that work is about  $5.7 \text{ km s}^{-1}$ . We also note that a high STT-induced DW speed of  $2.5 \text{ km s}^{-1}$  at a current density of  $1.2 \times 10^{12} \text{ A m}^{-2}$  was reported for  $\text{Mn}_{1-x}\text{Ni}_x\text{N}$  ferrimagnets without RE elements<sup>25</sup>. These results show the great potential of ferrimagnets as an excellent material platform for DW-based spintronic devices that can operate at room temperature.

We now turn to ferrimagnetic skyrmions. To realize skyrmion-based racetrack memories<sup>77</sup>, it is desirable to achieve small, room-temperature stable skyrmions that exhibit a zero skyrmion Hall angle. Their energetic stability derives from both the Dzyaloshinskii–Moriya interaction, which reduces the energy cost of a chiral texture, and the magnetostatic interactions, which enhance the stability through flux closure, but which also tend to result in large skyrmion sizes<sup>54,84</sup>. The low stray fields in ferrimagnets, combined with the bulk perpendicular anisotropy that allows for larger film thicknesses, were predicted and experimentally demonstrated<sup>20</sup> to allow for room-temperature stable skyrmions with sizes that approached 10 nm in a CoGd film imaged via element-resolved X-ray holography. These same films were shown to host DWs with compensated dynamics, which is an important step towards potential device applications based on ferrimagnetic textures.

Ferrimagnetic skyrmions have shown a large skyrmion Hall angle<sup>85,86</sup> ( $\theta_{\text{skH}} > 30^\circ$ ), which further hampers the development of skyrmion-based racetrack memories. Although antiferromagnetic skyrmions are expected to exhibit a zero  $\theta_{\text{skH}}$  owing to vanishing  $\delta_s$  (refs. <sup>87,88</sup>), this behaviour is not yet experimentally demonstrated. A series of breakthroughs on this issue came from experiments with compensated ferrimagnets. It was shown that  $\theta_{\text{skH}}$  can be reduced to  $\sim 20^\circ$  in ferrimagnet GdFeCo (Fig. 5a)<sup>89</sup>. The demonstration of a zero skyrmion Hall angle has been reported<sup>27</sup> by measuring the elongation angle of a magnetic bubble in GdFeCo at varying temperatures across  $T_A$  (Fig. 5b). The elongation direction is governed by a half-skyrmion motion at the front edge of the bubble and the elongation angle is thus identified as the skyrmion Hall angle of a half-skyrmion. Experimental results (Fig. 5b) show that the skyrmion Hall angle vanishes at  $T_A \approx 283$  K, regardless of the magnetization state (up or down), which corresponds to the skyrmion number  $Q = \pm 1/2$ , which is consistent with equation (6).

### Spin transport in compensated ferrimagnets

Another intriguing aspect of compensated ferrimagnets concerns the nature of spin transport, which is distinct from that of both ferromagnets and antiferromagnets. Conduction electron spins experience an antiferromagnetic coupling between RE  $5d$  spins and TM  $3d$  spins at the Fermi level. This picture is consistent with low-temperature measurements of  $P$  for RE and TM elements<sup>90</sup>:  $P$  of Gd is 0.13 whereas  $P$  of Co is 0.41. Given a larger Gd moment than Co moment at low temperatures, this low-temperature measurement shows that Gd  $4f$  spins, mainly responsible for the Gd moment, have a negligible interaction with the conduction electron spins. As a result,  $P$  is non-zero at both  $T_A$  and  $T_M$ . The non-negligible  $P$  of Gd<sup>90</sup> shows that the conduction electron spins interact not only with the Co  $3d$  spins, but also with the Gd  $5d$  spins. As a result, the conduction electron spins partly experience an antiferromagnet-like environment, which offers an experimental framework to study spin transport through effective antiferromagnetic order.

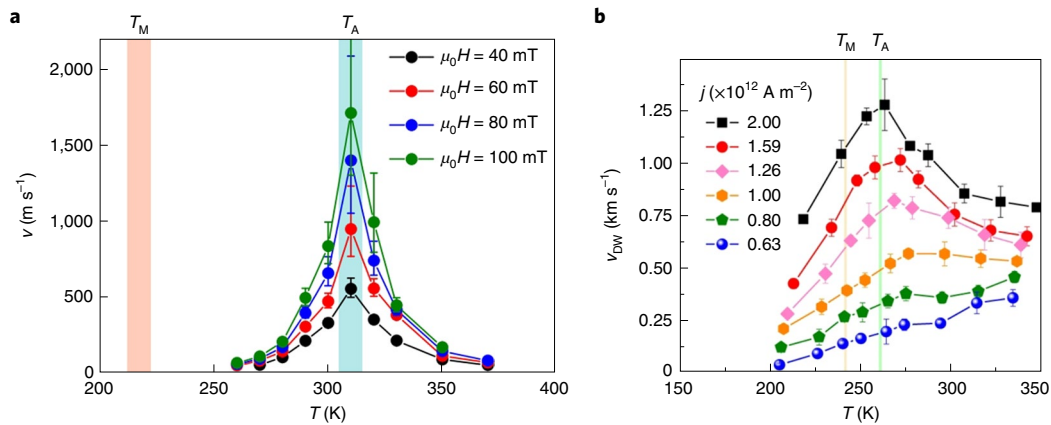


**Fig. 4 | Fast motion of ferrimagnetic DW at  $T_A$ .** **a**, Field-driven DW motion in a GdFeCo sample at various temperatures<sup>19</sup>. The DW velocity exhibits a maximum near 310 K, which is identified as  $T_A$ . **b**, SOT-driven DW motion in a GdCo sample at various temperatures<sup>20</sup>. The velocity is maximum at  $T_A \approx 260$  K.  $T_M$  is the magnetic moment compensation point at which net magnetic moment vanishes. Error bars represent the statistical standard error. Panel **a** adapted with permission from ref. <sup>19</sup>, Springer Nature Ltd. Panel **b** reproduced with permission from ref. <sup>20</sup>, Springer Nature Ltd.

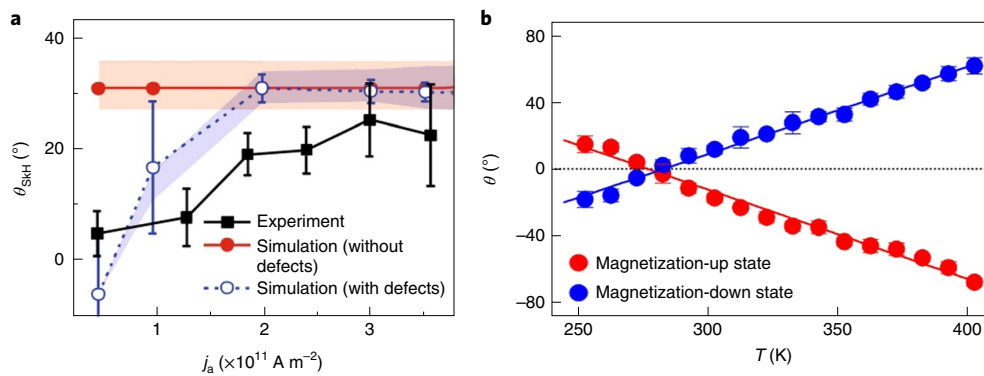


**Fig. 5 | Skyrmion Hall angle in ferrimagnets.** **a**,  $\theta_{\text{SkH}}$  of SOT-driven skyrmions in GdCo at various currents<sup>89</sup>. The black squares are experimental results. The filled (open) circles are simulation results without (with) defects.  $j_a$  is the applied current density. **b**, Temperature dependence of the half-skyrmion Hall angle  $\theta$  measured in the current-induced elongation of magnetic bubbles in GdFeCo (ref. <sup>27</sup>), which changes its sign across  $T_A \approx 280$  K. The red (blue) circles are experimental results for the elongation of the magnetization-up (-down) state. The lines are guides to the eye. Error bars represent the statistical standard error. Panels reproduced with permission from: **a**, ref. <sup>89</sup>, Springer Nature Ltd; **b**, ref. <sup>27</sup>, Springer Nature Ltd.

One of the physical quantities that can characterize the effect of the antiparallel exchange fields on spin transport is the so-called spin coherence length  $\lambda_c$ , the length scale over which a transverse spin current (that is, polarized perpendicularly to the background magnetic order) decays. In ferromagnets,  $\lambda_c$  is very short, for example, on the order of a few Ångströms in strong ferromagnets, such as Co or Fe, owing to a short spin precession length induced by the homogeneous strong exchange field (Fig. 6c). However, it was theoretically suggested that  $\lambda_c$  is long in antiferromagnets owing to the staggered order on the atomic scale<sup>91–93</sup> (Fig. 6d). A recent study of ferrimagnetic multilayers  $[\text{Co}/\text{Tb}]_N$ , where  $N$  represents the number of repetitions of Co/Tb, probed  $\lambda_c$  through spin-pumping experiments (Fig. 6e,f)<sup>30</sup>. The ferromagnetic  $[\text{Co}/\text{Ni}]_N$  or ferrimagnetic  $[\text{Co}/\text{Tb}]_N$  are magnetized perpendicularly (Fig. 6e). An in-plane magnetized top Co layer generates a spin-pumping-induced spin current polarized in the plane (thus a transverse spin current for the Co/Ni or Co/Tb magnetization), which passes through the Cu layer and enters  $[\text{Co}/\text{Ni}]_N$  or  $[\text{Co}/\text{Tb}]_N$ . The bottom Pt layer is used to detect the transverse spin current coming out of the multilayers via the inverse spin Hall voltage ( $V_{\text{ISHE}}$ ). Figure 6f shows that  $V_{\text{ISHE}}$  for a 0.9-nm-thick  $[\text{Co}/\text{Ni}]_N$  (blue triangles) is negligibly small, whereas  $V_{\text{ISHE}}$  for the 5.3-nm-thick  $[\text{Co}/\text{Tb}]_N$  (red circles) is substantial.

A vanishingly small  $V_{\text{ISHE}}$  for a Pt/[Co/Tb]/Cu stack without the top Co layer (green triangles) shows that the substantial  $V_{\text{ISHE}}$  is, indeed, due to the transverse spin current injected from the top Co layer. Combined with a negligible  $V_{\text{ISHE}}$  of Co/Tb<sup>30</sup>, this result shows that  $\lambda_c$  is longer in ferrimagnets than in ferromagnets. An independent experiment also showed that  $\lambda_c$  in CoGd alloys is about four to five times longer than that in ferromagnets<sup>31</sup>.

In ferromagnets, the short  $\lambda_c$  results in a  $1/d_M$  ( $d_M$ , thickness of the magnetic layer) dependence of the spin torque (either STT or SOT). As a result, more current is required to switch a thicker and more thermally stable ferromagnet. In contrast, the long  $\lambda_c$  weakens the  $1/d_M$  dependence. Indeed, SOT switching of a relatively thick ferrimagnet at a low current density was experimentally reported by several groups<sup>30,94–97</sup>. However, it is not straightforward to correlate the long  $\lambda_c$  directly with the switching experiments for the following reasons: current-induced Joule heating can largely modify the magnetic properties of ferrimagnets<sup>24,98</sup>, thickness-dependent variations of the magnetic properties also hamper a direct correlation<sup>30,99</sup> and, moreover, SOT in certain ferrimagnets is found to be most efficient at  $T_M$  (refs. <sup>94–97,100</sup>). This challenges the conventional picture of spin torques, in which the conduction electron spin interacts with the spin density (not the

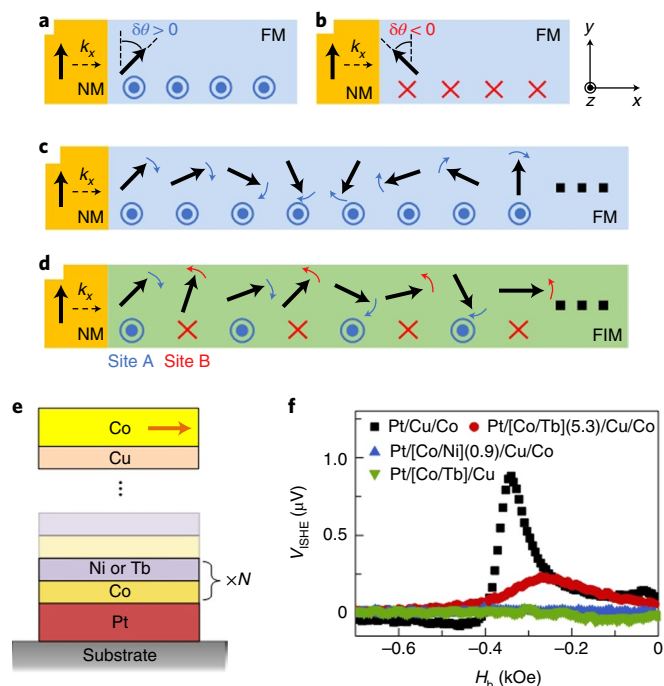


**Fig. 6 | Spin coherence length in a ferrimagnetic multilayer.** **a,b**, Local precession angle  $\delta\theta$  of spins injected from a normal metal (NM) at momentum  $k_x$  in a ferromagnet (FM) with magnetization up  $\mathbf{m} = \hat{\mathbf{z}}$  (**a**) and down  $\mathbf{m} = -\hat{\mathbf{z}}$  (**b**). **c**, Precession of an electron spin traversing through a FM, which is uniform due to the homogeneous exchange field from the local magnetic moments. **d**, Precession of an electron spin traversing through a ferrimagnet (FIM), which is staggered due to the antiparallel alignment of the neighbouring magnetic moments and thus partially cancelled out when averaged over a long distance. **e**, Schematic illustration of multilayer Pt/[Co/Ni]<sub>n</sub>/Cu/Co and Pt/[Co/Tb]<sub>n</sub>/Cu/Co for spin-pumping experiments, in which the top Co, which is magnetized in the plane, is used for spin pumping and the bottom Pt is used to detect the spin current. **f**, The  $V_{\text{SHE}}$  in Pt as a function of the in-plane bias field  $H_b$  for the reference sample Pt/Cu/Co, the ferrimagnetic multilayer Pt/[Co/Tb]<sub>n</sub>(5.3-nm-thick)/Cu/Co, the ferromagnetic multilayer Pt/[Co/Ni]<sub>n</sub>(0.9-nm-thick)/Cu/Co, and Pt/[Co/Tb]<sub>n</sub>/Cu without the top Co<sup>30</sup>. Figure reproduced with permission from ref. <sup>30</sup>, Springer Nature Ltd.

magnetic moment) at the Fermi level (not in the whole Fermi sea). These results demand further research efforts on the spin-torque switching of ferrimagnets.

The long  $\lambda_c$  of ferrimagnets is also related to the non-adiabaticity  $\beta$ , which corresponds to the non-adiabatic STT. The physics of  $\beta$  has been understood to a certain degree because, for ferromagnets, it is shown to be of the same order as the Gilbert damping  $\alpha$  (refs. <sup>101,102</sup>). However, a recent DW experiment using GdFeCo suggests<sup>32</sup> that the  $\beta$  physics in antiferromagnetically coupled systems is qualitatively different from that in ferromagnets. By analysing the current contribution to the DW velocity with equation (5),  $\beta$  was estimated to be about  $-0.5$ , which is far larger than  $\alpha$  ( $\sim 0.003$ ). This large  $\beta$  is attributed to the spin-mistracking process<sup>102,103</sup>, which was originally introduced to describe an enhanced  $\beta$  in ferromagnets, when the spin precession length is longer than the DW width. A recent theory showed that spin mistracking is more pronounced in antiferromagnets than in ferromagnets<sup>104</sup>, in line with the long  $\lambda_c$  in antiferromagnetically ordered systems. Quantitatively, however, the large  $\beta/\alpha$  ratio is poorly understood at this moment, and demands further theoretical studies on spin transport in compensated ferrimagnets.

## Outlook

We first comment on the potential concerns about ferrimagnets for practical applications and then discuss their opportunities. One concern is the strong temperature dependence of their magnetic properties, which is intrinsic to RE–TM ferrimagnets because of the highly localized RE 4*f* electrons and associated low Curie temperature of the RE elements. As any practical device must satisfy a desired performance in an  $\sim 100$  K range around room temperature, this strong temperature dependence is unwanted for applications. Then, the question is whether a physical quantity relevant to a specific device exceeds a target threshold in that 100 K range. Concerning DW devices, for instance, the answer would be yes: current-induced ferrimagnetic DW speeds exceed  $500 \text{ m s}^{-1}$ , which corresponds to an operation time of 0.2 ns for a 100-nm-long device, in a temperature range over 100 K (Fig. 4b)<sup>20</sup>. Another concern is about the reactivity of RE elements, especially with oxygen, which originates from a large negative enthalpy of formation of RE oxides<sup>105</sup>. A related concern is the material inhomogeneities in ferrimagnets<sup>99,105,106</sup>, which may cause a large diversity of experimental results. Given that RE–TM ferrimagnets have already been commercialized in various application areas<sup>2,4,5,7</sup>, such oxidation or inhomogeneity problems can be overcome by material and process engineering. However, the inhomogeneity issue might be turned into an advantage of ferrimagnets if a gradient of their magnetic properties could be obtained, as it would break the inversion symmetry of the systems. Combined with the large spin–orbit coupling expected in RE-based ferrimagnets, this allows for a bulk-like chiral exchange interaction<sup>107,108</sup>, and thus the stabilization of chiral spin textures in single ferrimagnetic films.

We next turn to the opportunities of ferrimagnet research. Although there have been rapid theoretical and experimental developments of ferrimagnetic spintronics over the past couple of years, the potential of ferrimagnets for spin-based information processing technologies has just started to be explored and there are many unanswered questions and unachieved goals, some of which are addressed below.

Concerning the high-energy longitudinal dynamics, there is currently an ongoing effort to find the optimal parameters for single-shot helicity-independent AOS in generic ferrimagnets<sup>13</sup>, which is expected to have the capability to yield high-density storage media with storage densities that surpass  $0.6 \text{ Tb cm}^{-2}$ . In addition, AOS has been demonstrated<sup>48</sup> to be not only fast but also energy efficient: a  $20 \times 20 \text{ nm}^2$  bit requires about 10 fJ. The introduction of an optically switchable layer in a magnetic random-access memory was successfully demonstrated<sup>49</sup>. Further research is required to bring this demonstration towards actual applications, in which bringing photons efficiently to magnetic random-access memory cells is a major challenge.

Concerning low-energy transversal dynamics, the high speed of ferrimagnetic textures, higher than that of ferromagnetic textures, is one of the most vivid advantages of ferrimagnets. The reported record DW velocity in ferrimagnets has been steadily increasing<sup>19,20,24</sup>. Given the DW velocity, an important question arises: what is the highest velocity of current-induced DW motion? This question was addressed by an experiment<sup>109</sup> on SOT-driven DW motion in a ferrimagnetic Bi-doped yttrium iron garnet near the angular-momentum-compensation condition. This experiment demonstrated that the DW dynamics becomes relativistic when the current-driven DW speed approaches the maximum magnon group velocity, which sets the upper limit of the DW speed, consistent with theoretical predictions<sup>110,111</sup>. In contrast with several available reports on the fast DW dynamics at  $T_A$ , an experimental demonstration of fast skyrmion motion with a vanishing skyrmion Hall effect near  $T_A$  has not been achieved yet. Given that the skyrmion size in ferrimagnets can be as small as 10 nm (ref. <sup>20</sup>), achieving a fast Hall-effect-free skyrmion motion would offer a

**Table 1 | List of possible research directions using ferrimagnets**

Research directions	Specific topics
New materials	Ferrimagnetic insulators Synthetic ferrimagnets Non-collinear ferrimagnets Ferrimagnets with strong spin-orbit coupling Ferrimagnets with ultrasmall damping Ferrimagnets with room-temperature compensation points
Fundamental studies	Dynamics of spin textures (DWs, skyrmions, vortices, Bloch points and stripes) faster than those in ferromagnets Spin waves with distinct handedness Interaction between spin textures and spin waves Interplay of charge, spin and heat in ferrimagnets Transport phenomena (spin torque, magnetoresistance and various Hall effects) Sperimagnetism
Practical applications	Ultrafast magneto-optical recording Soliton-based racetrack memory Wave-based computing with spin waves of distinct handedness Quantum information processing Neuromorphic computing

strong thrust for the development of skyrmion-based high-density spintronic devices.

The transport of conduction electron spins in ferrimagnets is even less explored. In addition to the questions for SOT switching and a large  $|\beta|/\alpha$  in ferrimagnets, an interesting question is how to exploit the large spin-orbit coupling of RE elements for charge-to-spin interconversion. Theories<sup>112–114</sup> predict that spin currents can be efficiently generated in magnetic materials with spin-orbit coupling, which have been confirmed experimentally using standard ferromagnets<sup>115–117</sup>. However, given the large spin-orbit coupling related to the presence of RE elements, ferrimagnets might be the most promising systems for the generation of large spin currents and hence large associated SOT, as currently investigated<sup>108,118</sup>.

Also, charge and spin are not the only degrees of freedom that can flow through ferrimagnets. Another field in which ferrimagnets are welcomed is magnonics, where spin waves, or their quanta called magnons, are utilized to carry and process information<sup>3,119–121</sup>. Ferrimagnets are expected to offer novel magnonic phenomena through the unique combination of antiferromagnetic-like dynamics and ferromagnetic-like controllability, as suggested in recent reports of the observation of two distinct handednesses of spin waves in ferrimagnets<sup>65,122,123</sup>. Spin caloritronics<sup>124</sup>, which exploits the spin Seebeck effect<sup>125</sup>, is another field in which magnon transport is important. A main material for spin caloritronics and magnonics has been yttrium iron garnet, an insulating ferrimagnet<sup>126,127</sup>. However, yttrium iron garnet has a very limited tunability of magnetization and angular momentum. Experiments on RE-doped garnets<sup>109,128</sup> suggest ways to improve the tunability, which allows one to explore and exploit the interplay of heat and magnons in the vicinity of the two compensation points.

Going beyond the specific field of ferrimagnetic spintronics, introducing ferrimagnets as a tunable material platform is expected to make a notable impact on other branches of spintronics. One such field is cavity spintronics<sup>129</sup>, which aims to exploit the interaction between spins and photons to develop a new information-processing technology. Compensated ferrimagnets with different  $T_A$  and  $T_M$  are expected to enhance the coupling at  $T_A$  owing to a concerted action of a finite net magnetization and magnon squeezing<sup>130</sup>. This also

offers a high excitation frequency that expands the frequency window in which the transduction of information occurs<sup>130,131</sup>.

The introduction of ferrimagnets in spintronics has already made an appreciable impact on spintronics and magnetism, with novel dynamics and transport phenomena as discussed above. However, there are much wider unexplored areas in ferrimagnetic spintronics than those investigated so far (Table 1). The ultimate source of the unique nature of ferrimagnets is their multiple magnetic elements with distinct properties (Fig. 1b), which include the gyromagnetic ratio (giving rise to the separation of  $T_A$  and  $T_M$ ) and transport. As shown in Fig. 1c, this wide parameter space provides a large set of yet-unexplored ferrimagnetic alloys with various element choices and compositions, and led to extraordinary findings for fast dynamics, efficient spin transport and other branches of spintronics and magnetism. Ever since the beginning of spintronics with ferromagnets, the material platform for spintronics has been expanding in several directions, which include antiferromagnets, non-collinear magnets and, currently, ferrimagnets, through which we have been witnessing the discovery of unexpected phenomena. We cannot wait to see what will be discovered in spintronics in the coming years through thorough studies of ferrimagnets, and, beyond, what nature will offer us for the next-generation spin-based information-processing technologies in the coming decades.

Received: 9 November 2020; Accepted: 21 September 2021;  
Published online: 23 December 2021

## References

- Néel, L. Antiferromagnetism and ferrimagnetism. *Proc. Phys. Soc. A* **65**, 869 (1952).
- Dionne, G. F. A review of ferrites for microwave applications. *Proc. IEEE* **63**, 777–789 (1975).
- Serga, A. A., Chumak, A. V. & Hillebrands, B. YIG magnonics. *J. Phys. D* **43**, 264002 (2010).
- Chaudhari, P., Cuomo, J. J. & Gambino, R. J. Amorphous metallic films for magneto-optic applications. *Appl. Phys. Lett.* **42**, 202 (1973).
- Carey, R., Newman, D. M. & Thomas, B. W. J. Magneto-optic recording. *J. Phys. D* **28**, 2207–2227 (1995).
- Hansen, P. et al. Magnetic and magneto-optical properties of rare-earth transition-metal alloys containing Gd, Tb, Fe, Co. *J. Appl. Phys.* **66**, 756 (1989).
- Tsunashima, S. Magneto-optical recording. *J. Phys. D* **34**, R87–R102 (2001).
- Focus on antiferromagnetic spintronics. *Nat. Phys.* <https://www.nature.com/collections/wpplmmvnt> (2018).
- Baltz, V. et al. Antiferromagnetic spintronics. *Rev. Mod. Phys.* **90**, 015005 (2018).
- Stanciu, C. D. et al. All-optical magnetic recording with circularly polarized light. *Phys. Rev. Lett.* **99**, 047601 (2007).
- Radu, I. et al. Transient ferromagnetic-like state mediating ultrafast reversal of antiferromagnetically coupled spins. *Nature* **472**, 205–208 (2011).
- Mentink, J. H. et al. Ultrafast spin dynamics in multisublattice magnets. *Phys. Rev. Lett.* **108**, 057202 (2012).
- Davies, C. S. et al. Pathways for single-shot all-optical switching of magnetization in ferrimagnets. *Phys. Rev. Appl.* **13**, 024064 (2020).
- Ostler, T. A. et al. Ultrafast heating as a sufficient stimulus for magnetization reversal in a ferrimagnet. *Nat. Commun.* **3**, 666 (2012).
- Evans, R. F. L., Ostler, T. A., Chantrell, R. W., Radu, I. & Rasing, T. Ultrafast thermally induced magnetic switching in synthetic ferrimagnets. *Appl. Phys. Lett.* **104**, 082410 (2014).
- Mangin, S. et al. Engineered materials for all-optical helicity-dependent magnetic switching. *Nat. Mater.* **13**, 286–292 (2014).
- Beaurepaire, E., Merle, J.-C., Daunois, A. & Bigot, J.-Y. Ultrafast spin dynamics in ferromagnetic nickel. *Phys. Rev. Lett.* **76**, 4250–4253 (1996).
- Hennecke, M. et al. Angular momentum flow during ultrafast demagnetization of a ferrimagnet. *Phys. Rev. Lett.* **122**, 157202 (2019).
- Kim, K.-J. et al. Fast domain wall motion in the vicinity of the angular momentum compensation temperature of ferrimagnets. *Nat. Mater.* **16**, 1187–1192 (2017).
- Caretta, L. et al. Fast current-driven domain walls and small skyrmions in a compensated ferrimagnet. *Nat. Nanotechnol.* **13**, 1154–1160 (2018).
- Siddiqui, S. A., Han, J., Finley, J. T., Ross, C. A. & Liu, L. Current-induced domain wall motion in a compensated ferrimagnet. *Phys. Rev. Lett.* **121**, 057701 (2018).

22. Bläsing, R. et al. Exchange coupling torque in ferrimagnetic Co/Gd bilayer maximized near angular momentum compensation temperature. *Nat. Commun.* **9**, 4984 (2018).
23. Avci, C. O. et al. Interface-driven chiral magnetism and current-driven domain walls in insulating magnetic garnets. *Nat. Nanotechnol.* **14**, 561–566 (2019).
24. Cai, K. et al. Ultrafast and energy-efficient spin-orbit torque switching in compensated ferrimagnets. *Nat. Electron.* **3**, 37–42 (2020).
25. Ghosh, S. et al. Current-driven domain wall dynamics in ferrimagnetic nickel-doped Mn<sub>2</sub>N films: very large domain wall velocities and reversal of motion direction across the magnetic compensation point. *Nano Lett.* **21**, 2580–2587 (2021).
26. Kim, S. K., Lee, K.-J. & Tserkovnyak, Y. Self-focusing skyrmion racetracks in ferrimagnets. *Phys. Rev. B* **95**, 140404(R) (2017).
27. Hirata, Y. et al. Vanishing skyrmion Hall effect at the angular momentum compensation temperature of a ferrimagnet. *Nat. Nanotechnol.* **14**, 232–236 (2019).
28. Oh, S.-H. et al. Coherent terahertz spin-wave emission associated with ferrimagnetic domain walls. *Phys. Rev. B* **96**, 100407(R) (2017).
29. Oh, S.-H. & Lee, K.-J. Ferrimagnetic domain wall motion induced by damping-like spin-orbit torque. *J. Magn.* **23**, 196–200 (2018).
30. Yu, J. et al. Long spin coherence length and bulk-like spin-orbit torque in ferrimagnetic multilayers. *Nat. Mater.* **18**, 29–34 (2019).
31. Lim, Y. et al. Dephasing of transverse spin current in ferrimagnetic alloys. *Phys. Rev. B* **103**, 024443 (2021).
32. Okuno, T. et al. Spin-transfer torques for domain wall motion in antiferromagnetically coupled ferrimagnets. *Nat. Electron.* **2**, 389–393 (2019).
33. Koopmans, B., Ruigrok, J. J. M., Dalla Longa, F. & de Jonge, W. J. M. Unifying ultrafast magnetization dynamics. *Phys. Rev. Lett.* **95**, 267207 (2005).
34. Singh, N., Elliott, P., Dewhurst, J. K., Gross, E. K. U. & Sharma, S. Ab-initio real-time magnon dynamics in ferromagnetic and ferrimagnetic systems. *Phys. Status Solidi B* **257**, 1900654 (2020).
35. Koopmans, B. et al. Explaining the paradoxical diversity of ultrafast laser-induced demagnetization. *Nat. Mater.* **9**, 259–265 (2010).
36. Wietstruck, M. et al. Hot-electron-driven enhancement of spin-lattice coupling in Gd and Tb 4f ferromagnets observed by femtosecond X-ray magnetic circular dichroism. *Phys. Rev. Lett.* **106**, 127401 (2011).
37. Radu, I. et al. Ultrafast and distinct spin dynamics in magnetic alloys. *Spin* **5**, 1550004 (2015).
38. Mentink, J. *Magnetism on the Timescale of the Exchange Interaction: Explanations and Predictions*. PhD thesis, Radboud Univ. (2012).
39. Campbell, I. A. Indirect exchange for rare earths in metals. *J. Phys. F* **2**, L47 (1972).
40. Buschow, K. H. J. Intermetallic compounds of rare-earth and 3d transition metals. *Rep. Prog. Phys.* **40**, 1179 (1977).
41. Lang, J. K., Baer, Y. & Cox, P. A. Study of the 4f levels in rare-earth metals by high-energy spectroscopies. *Phys. Rev. Lett.* **42**, 74 (1979).
42. Bar'yakhtar, V. G. Phenomenological description of relaxation processes in magnetic materials. *Sov. Phys. JETP* **60**, 863–867 (1984).
43. Bar'yakhtar, V. G. Crystal symmetry and the structure of the relaxation terms in the antiferromagnet dynamic equations of motion. *Sov. Phys. JETP* **67**, 757 (1988).
44. Bar'yakhtar, V. G., Butrim, V. I. & Ivanov, B. A. Exchange relaxation as a mechanism of the ultrafast reorientation of spins in a two-sublattice ferrimagnet. *JETP Lett.* **98**, 289–293 (2013).
45. Wienholdt, S., Hinze, D., Carva, K., Oppeneer, P. M. & Nowak, U. Orbital-resolved spin model for thermal magnetization switching in rare-earth-based ferrimagnets. *Phys. Rev. B* **88**, 020406(R) (2013).
46. Schellekens, A. J. & Koopmans, B. Microscopic model for ultrafast magnetization dynamics of multisublattice magnets. *Phys. Rev. B* **87**, 020407(R) (2013).
47. Barker, J. & Atxitia, U. A review of modelling in ferrimagnetic spintronics. *J. Phys. Soc. Jpn* **90**, 081001 (2021).
48. Laliou, M. L. M., Peeters, M. J. G., Haenen, S. R. R., Lavrijsen, R. & Koopmans, B. Deterministic all-optical switching of synthetic ferrimagnets using single femtosecond laser pulses. *Phys. Rev. B* **96**, 220411(R) (2017).
49. Avilés-Félix, L. et al. Single-shot all-optical switching of magnetization in Tb/Co multilayer-based electrodes. *Sci. Rep.* **10**, 5211 (2020).
50. Khorsand, A. R. et al. Role of magnetic circular dichroism in all-optical magnetic recording. *Phys. Rev. Lett.* **108**, 127205 (2012).
51. Atxitia, U., Barker, J., Chantrell, R. W. & Chubykalo-Fesenko, O. Controlling the polarity of the transient ferromagnetic-like state in ferrimagnets. *Phys. Rev. B* **89**, 224421 (2014).
52. Steil, D., Alebrand, S., Hassdenteufel, A., Cinchetti, M. & Aeschlimann, M. All-optical magnetization recording by tailoring optical excitation parameters. *Phys. Rev. B* **84**, 224408 (2011).
53. Yang, Y. et al. Ultrafast magnetization reversal by picosecond electrical pulses. *Sci. Adv.* **3**, e1603117 (2017).
54. Finazzi, M. et al. Laser-induced magnetic nanostructures with tunable topological properties. *Phys. Rev. Lett.* **110**, 177205 (2013).
55. Banerjee, C. et al. Single pulse all-optical toggle switching of magnetization without gadolinium in the ferrimagnet Mn<sub>2</sub>Ru<sub>2</sub>Ga. *Nat. Commun.* **11**, 4444 (2020).
56. Davies, C. S. et al. Exchange-driven all-optical magnetic switching in compensated 3d ferrimagnets. *Phys. Rev. Res.* **2**, 032044(R) (2020).
57. Stupakiewicz, A., Szerenos, K., Afanasiev, D., Kirilyuk, A. & Kimel, A. V. Ultrafast nonthermal photo-magnetic recording in a transparent medium. *Nature* **542**, 71–74 (2017).
58. Wang, S. et al. Dual-shot dynamics and ultimate frequency of all-optical magnetic recording on GdFeCo. *Light Sci. Appl.* **10**, 8 (2021).
59. El-Ghazaly, A. et al. Ultrafast magnetization switching in nanoscale magnetic dots. *Appl. Phys. Lett.* **114**, 232407 (2019).
60. Ivanov, B. A. & Sukstanskii, A. L. Nonlinear magnetization waves in ferrites. *Sov. Phys. JETP* **57**, 214 (1983).
61. Chiolerio, A. & Loss, D. Macroscopic quantum coherence in ferrimagnets. *Phys. Rev. B* **56**, 738 (1997).
62. Kimel, A. V. et al. Inertia-driven spin switching in antiferromagnets. *Nat. Phys.* **5**, 727–731 (2009).
63. Binder, M. et al. Magnetization dynamics of the ferrimagnet CoGd near the compensation of magnetization and angular momentum. *Phys. Rev. B* **74**, 134404 (2006).
64. Okuno, T. et al. Temperature dependence of magnetic resonance in ferrimagnetic GdFeCo alloys. *Appl. Phys. Express* **12**, 093001 (2019).
65. Kim, C. et al. Spin wave excitation with distinct handedness across compensation temperatures of ferrimagnets. *Nat. Mater.* **19**, 980–985 (2020).
66. Schryer, N. & Walker, L. The motion of 180° domain walls in uniform dc magnetic fields. *J. Appl. Phys.* **45**, 5406–5421 (1974).
67. Beach, G., Nistor, C., Knutson, C., Tsoi, M. & Erskine, J. Dynamics of field-driven domain-wall propagation in ferromagnetic nanowires. *Nat. Mater.* **4**, 741–744 (2005).
68. Mougín, A., Cormier, M., Adam, J. P., Metaxas, P. J. & Ferré, J. Domain wall mobility, stability and Walker breakdown in magnetic nanowires. *Europhys. Lett.* **78**, 57007 (2007).
69. Bar'yakhtar, V. G., Ivanov, B. A. & Chetkin, M. V. Dynamics of domain walls in weak ferromagnets. *Sov. Phys. Usp.* **28**, 563–588 (1985).
70. Tveten, E. G., Qaiumzadeh, A., Tretiakov, O. A. & Brataas, A. Staggered dynamics in antiferromagnets by collective coordinates. *Phys. Rev. Lett.* **110**, 127208 (2013).
71. Hals, K. M. D., Tserkovnyak, Y. & Brataas, A. Phenomenology of current-induced dynamics in antiferromagnets. *Phys. Rev. Lett.* **106**, 107206 (2011).
72. Rößler, U. K., Bogdanov, A. N. & Pfleiderer, C. Spontaneous skyrmion ground states in magnetic metals. *Nature* **442**, 797–801 (2006).
73. Mühlbauer, S. et al. Skyrmion lattice in a chiral magnet. *Science* **323**, 915–919 (2009).
74. Yu, X. Z. et al. Real-space observation of a two-dimensional skyrmion crystal. *Nature* **465**, 901–904 (2010).
75. Dzialoshinskii, I. E. Thermodynamic theory of weak ferromagnetism in antiferromagnetic substances. *Sov. Phys. JETP* **5**, 1259–1272 (1957).
76. Moriya, T. Anisotropic superexchange interaction and weak ferromagnetism. *Phys. Rev.* **120**, 91–98 (1960).
77. Fert, A., Reyren, N. & Cros, V. Magnetic skyrmions: advances in physics and potential applications. *Nat. Rev. Mater.* **2**, 17031 (2017).
78. Jiang, W. et al. Blowing magnetic skyrmion bubbles. *Science* **349**, 283–286 (2015).
79. Woo, S. et al. Observation of room-temperature magnetic skyrmions and their current-driven dynamics in ultrathin metallic ferromagnets. *Nat. Mater.* **15**, 501–506 (2016).
80. Moreau-Luchaire, C. et al. Additive interfacial chiral interaction in multilayers for stabilization of small individual skyrmions at room temperature. *Nat. Nanotechnol.* **11**, 444–448 (2016).
81. Boule, O. et al. Room-temperature chiral magnetic skyrmions in ultrathin magnetic nanostructures. *Nat. Nanotechnol.* **11**, 449–454 (2016).
82. Büttner, F. et al. Field-free deterministic ultrafast creation of magnetic skyrmions by spin-orbit torques. *Nat. Nanotechnol.* **12**, 1040–1044 (2017).
83. Pollard, S. D. et al. Observation of stable Néel skyrmions in cobalt/palladium multilayers with Lorentz transmission electron microscopy. *Nat. Commun.* **8**, 14761 (2017).
84. Büttner, F., Lemesch, I. & Beach, G. S. D. Theory of isolated magnetic skyrmions: from fundamentals to room temperature applications. *Sci. Rep.* **8**, 4464 (2018).
85. Jiang, W. et al. Direct observation of the skyrmion Hall effect. *Nat. Phys.* **13**, 162–169 (2016).
86. Litzius, K. et al. Skyrmion Hall effect revealed by direct time-resolved X-ray microscopy. *Nat. Phys.* **13**, 170–175 (2016).
87. Barker, J. & Tretiakov, O. Static and dynamical properties of antiferromagnetic skyrmions in the presence of applied current and temperature. *Phys. Rev. Lett.* **116**, 147203 (2016).

88. Zhang, X., Zhou, Y. & Ezawa, M. Magnetic bilayer-skyrmions without skyrmion Hall effect. *Nat. Commun.* **7**, 10293 (2016).
89. Woo, S. et al. Current-driven dynamics and inhibition of the skyrmion Hall effect of ferrimagnetic skyrmions in GdFeCo films. *Nat. Commun.* **9**, 959 (2018).
90. Kaiser, C., Panchula, A. F. & Parkin, S. S. P. Finite tunneling spin polarization at the compensation point of rare-earth-metal–transition-metal alloys. *Phys. Rev. Lett.* **95**, 047202 (2005).
91. Núñez, A. S., Duine, R. A., Haney, P. & MacDonald, A. H. Theory of spin torques and giant magnetoresistance in antiferromagnetic metals. *Phys. Rev. B* **73**, 214426 (2006).
92. Haney, P. M. & MacDonald, A. H. Current-induced torques due to compensated antiferromagnets. *Phys. Rev. Lett.* **100**, 196801 (2008).
93. Xu, Y., Wang, S. & Xia, K. Spin-transfer torques in antiferromagnetic metals from first principles. *Phys. Rev. Lett.* **100**, 226602 (2008).
94. Mishra, R. et al. Anomalous current-induced spin torques in ferrimagnets near compensation. *Phys. Rev. Lett.* **118**, 167201 (2017).
95. Finley, J. & Liu, L. Spin-orbit-torque efficiency in compensated ferrimagnetic cobalt-terbium alloys. *Phys. Rev. Appl.* **6**, 054001 (2016).
96. Roschewsky, N., Lambert, C.-H. & Salahuddin, S. Spin-orbit torque switching of ultralarge-thickness ferrimagnetic GdFeCo. *Phys. Rev. B* **96**, 064406 (2017).
97. Ueda, K., Mann, M., de Brouwer, P. W. P., Bono, D. & Beach, G. S. D. Temperature dependence of spin-orbit torques across the magnetic compensation point in a ferrimagnetic TbCo alloy film. *Phys. Rev. B* **96**, 064410 (2017).
98. Pham, T. H. et al. Thermal contribution to the spin-orbit torque in metallic-ferrimagnetic systems. *Phys. Rev. Appl.* **9**, 064032 (2018).
99. Hebler, B., Hassdenteufel, A., Reinhardt, P., Karl, H. & Albrecht, M. Ferrimagnetic Tb–Fe alloy thin films: composition and thickness dependence of magnetic properties and all-optical switching. *Front. Mater.* **3**, 8 (2016).
100. Je, S.-G. et al. Spin-orbit torque-induced switching in ferrimagnetic alloys: experiments and modeling. *Appl. Phys. Lett.* **112**, 062401 (2018).
101. Tataru, G., Kohno, H. & Shibata, J. Microscopic approach to current-driven domain wall dynamics. *Phys. Rep.* **468**, 213–301 (2008).
102. Lee, K.-J. et al. Self-consistent calculation of spin transport and magnetization dynamics. *Phys. Rep.* **531**, 89–113 (2013).
103. Xiao, J., Zangwill, A. & Stiles, M. D. Spin-transfer torque for continuously variable magnetization. *Phys. Rev. B* **73**, 054428 (2006).
104. Park, H.-J. et al. Numerical computation of spin-transfer torques for antiferromagnetic domain walls. *Phys. Rev. B* **101**, 144431 (2020).
105. Kim, J. H. et al. Spin-orbit torques associated with ferrimagnetic order in Pt/GdFeCo/MgO layers. *Sci. Rep.* **8**, 6017 (2018).
106. Haltz, E. et al. Deviations from bulk behavior in TbFe(Co) thin films: interfaces contribution in the biased composition. *Phys. Rev. Mater.* **2**, 104410 (2018).
107. Kim, D.-H. et al. Bulk Dzyaloshinskii–Moriya interaction in amorphous ferrimagnetic alloys. *Nat. Mater.* **18**, 685–690 (2019).
108. Krishnia, S. et al. Making spin-orbit coupling visible in single layer ferrimagnets: direct observation of spin-orbit torques and chiral spin textures. *Phys. Rev. Appl.* **16**, 024040 (2021).
109. Caretta, L. et al. Relativistic kinematics of a magnetic soliton. *Science* **370**, 1438–1442 (2020).
110. Gomonay, O., Jungwirth, T. & Sinova, J. High antiferromagnetic domain wall velocity induced by Néel spin-orbit torques. *Phys. Rev. Lett.* **117**, 017202 (2016).
111. Shiino, T. et al. Antiferromagnetic domain wall motion by spin-orbit torques. *Phys. Rev. Lett.* **117**, 087203 (2016).
112. Taniguchi, T., Grollier, J. & Stiles, M. D. Spin-transfer torques generated by the anomalous Hall effect and anisotropic magnetoresistance. *Phys. Rev. Appl.* **3**, 044001 (2015).
113. Amin, V. P., Li, J., Stiles, M. D. & Haney, P. M. Intrinsic spin currents in ferromagnets. *Phys. Rev. B* **99**, 220405(R) (2019).
114. Kim, K.-W. & Lee, K.-J. Generalized spin drift-diffusion formalism in the presence of spin-orbit interaction of ferromagnets. *Phys. Rev. Lett.* **125**, 207205 (2020).
115. Baek, S.-H. C. et al. Spin currents and spin-orbit torques in ferromagnetic trilayers. *Nat. Mater.* **17**, 509–513 (2018).
116. Iihama, S. et al. Spin-transfer torque induced by the spin anomalous Hall effect. *Nat. Electron.* **1**, 120–123 (2018).
117. Wang, W. et al. Anomalous spin-orbit torques in magnetic single-layer films. *Nat. Nanotechnol.* **14**, 819–824 (2019).
118. Céspedes-Berrocal, D. et al. Current-induced spin torques on single GdFeCo magnetic layers. *Adv. Mater.* **33**, 2007047 (2021).
119. Krygylak, V. V., Demokritov, S. O. & Grundler, D. Magnonics. *J. Phys. D* **43**, 264001 (2010).
120. Lenk, B., Ulrichs, H., Garbs, F. & Münzenberg, M. The building blocks of magnonics. *Phys. Rep.* **507**, 107–136 (2011).
121. Chumak, A. V., Vasyuchka, V. I., Serga, A. A. & Hillebrands, B. Magnon spintronics. *Nat. Phys.* **11**, 453–461 (2015).
122. Liensberger, L. et al. Exchange-enhanced ultrastrong magnon–magnon coupling in a compensated ferrimagnet. *Phys. Rev. Lett.* **123**, 117204 (2019).
123. Nambu, Y. et al. Observation of magnon polarization. *Phys. Rev. Lett.* **125**, 027201 (2020).
124. Bauer, G. E. W., Saitoh, E. & van Wees, B. J. Spin caloritronics. *Nat. Mater.* **11**, 391–399 (2012).
125. Uchida, K. et al. Observation of the spin-Seebeck effect. *Nature* **455**, 778–781 (2008).
126. Uchida, K. et al. Observation of longitudinal spin-Seebeck effect in magnetic insulators. *Appl. Phys. Lett.* **97**, 172505 (2010).
127. Geprägs, S. et al. Origin of the spin Seebeck effect in compensated ferrimagnets. *Nat. Commun.* **7**, 10452 (2016).
128. Bauer, J. J. et al. Dysprosium iron garnet thin films with perpendicular magnetic anisotropy on silicon. *Adv. Electron. Mater.* **6**, 1900820 (2020).
129. Hu, C.-M. Dawn of cavity spintronics. *Phys. Can.* **72**, 76 (2016).
130. Shim, J.-C., Kim, S.-J., Kim, S. K. & Lee, K.-J. Enhanced magnon–photon coupling at the angular momentum compensation point of ferrimagnets. *Phys. Rev. Lett.* **125**, 027205 (2020).
131. Huang, M. et al. Voltage control of ferrimagnetic order and voltage-assisted writing of ferrimagnetic spin textures. *Nat. Nanotechnol.* **16**, 981–988 (2021).
132. Swaving, A. C. & Duine, R. A. Current-induced torques in continuous antiferromagnetic textures. *Phys. Rev. B* **83**, 054428 (2011).

## Acknowledgements

K.-J.L. acknowledges support from the Samsung Research Funding Center of Samsung Electronics under project no. SRFCMA1702-02. T.R. acknowledges support from the Nederlandse Organisatie voor Wetenschappelijk Onderzoek (NWO) through the programme Exciting Exchange, the European Union Horizon 2020 and the innovation programme under the FET-Open grand agreement no. 713481 (SPICE), and the European Research Council ERC grant agreement no. 856538 (3D MAGIC). H.Y. is supported by SpOT-LITE programme (A\*STAR grant, A18A6b0057) through RIE2020 funds, Samsung Electronics' University R&D programme (Exotic SOT materials/SOT characterization) and a National Research Foundation (NRF) Singapore Investigatorship (NRF106-2020-0015). G.S.D.B. acknowledges support through the DARPA 'Topological Excitations in Electronics (TEE)' programme. S.K.K. is supported by Brain Pool Plus Program through the National Research Foundation of Korea funded by the Ministry of Science and ICT (NRF-2020H1D3A2A03099291) and the National Research Foundation of Korea funded by the Korea Government via the SRC Center for Quantum Coherence in Condensed Matter (NRF-2016R1A5A1008184).

## Author contributions

The manuscript was written through contributions from all authors.

## Competing interests

The authors declare no competing interests.

## Additional information

Correspondence should be addressed to Kyung-Jin Lee.

**Peer review information** *Nature Materials* thanks Uwe Bovensiepen and the other, anonymous, reviewer(s) for their contribution to the peer review of this work.

**Reprints and permissions information** is available at [www.nature.com/reprints](http://www.nature.com/reprints).

**Publisher's note** Springer Nature remains neutral with regard to jurisdictional claims in published maps and institutional affiliations.

© Springer Nature Limited 2021